2018

Structure-based discovery of glycomimetic FmlH ligands as inhibitors of bacterial adhesion during urinary tract infection

Vasilios Kalas
Washington University School of Medicine in St. Louis

Michael E. Hibbing
Washington University School of Medicine in St. Louis

Amarendar Reddy Maddirala
Washington University School of Medicine in St. Louis

Ryan Chugani
Washington University School of Medicine in St. Louis

Jerome S. Pinkner
Washington University School of Medicine in St. Louis

See next page for additional authors

Recommended Citation

Kalas, Vasilios; Hibbing, Michael E.; Maddirala, Amarendar Reddy; Chugani, Ryan; Pinkner, Jerome S.; Mydock-McGrane, Laurel K.; Conover, Matt S.; Janetka, James W.; and Hultgren, Scott J., "Structure-based discovery of glycomimetic FmlH ligands as inhibitors of bacterial adhesion during urinary tract infection." Proceedings of the National Academy of Sciences of the United States of America. 115, 12. E2819-E2828. (2018).
https://digitalcommons.wustl.edu/open_access_pubs/6722

Structure-based discovery of glycomimetic FmlH ligands as inhibitors of bacterial adhesion during urinary tract infection

Vasilios Kalas[a,b,c], Michael E. Hibbing[a,b], Amarendar Reddy Maddirala[c], Ryan Chugani[c], Jerome S. Pinkner[a,b], Laurel K. Mydock-McGrane[c], Matt S. Conover[a,b], James W. Janetka[a,c,1], and Scott J. Hultgren[a,b,1]

[a]Center for Women's Infectious Disease Research, Washington University School of Medicine, St. Louis, MO 63110; [b]Department of Molecular Microbiology, Washington University School of Medicine, St. Louis, MO 63110; and [c]Department of Biochemistry and Molecular Biophysics, Washington University School of Medicine, St. Louis, MO 63110

Edited by Roy Curtiss III, University of Florida, Gainesville, FL, and approved February 13, 2018 (received for review November 20, 2017)

Treatment of bacterial infections is becoming a serious clinical challenge due to the global dissemination of multidrug antibiotic resistance, necessitating the search for alternative treatments to disarm the virulence mechanisms underlying these infections. Uropathogenic *Escherichia coli* (UPEC) employs multiple chaperone–usher pathway pili tipped with adhesins with diverse receptor specificities to colonize various host tissues and habitats. For example, UPEC F9 pili specifically bind galactose or *N*-acetylgalactosamine epitopes on the kidney and inflamed bladder. Using X-ray structure-guided methods, virtual screening, and multiplex ELISA arrays, we rationally designed aryl galactosides and *N*-acetylgalactosaminosides that inhibit the F9 pilus adhesin FmlH. The lead compound, 29β-NAc, is a biphenyl *N*-acetyl-β-galactosaminoside with a K_i of ∼90 nM, representing a major advancement in potency relative to the characteristically weak nature of most carbohydrate–lectin interactions. 29β-NAc binds tightly to FmlH by engaging the residues Y46 through edge-to-face π-stacking with its A-phenyl ring, R142 in a salt-bridge interaction with its carboxylate group, and K132 through water-mediated hydrogen bonding with its N-acetyl group. Administration of 29β-NAc in a mouse urinary tract infection (UTI) model significantly reduced bladder and kidney bacterial burdens, and coadministration of 29β-NAc and mannoside 4Z269, which targets the type 1 pilus adhesin FimH, resulted in greater elimination of bacteria from the urinary tract than either compound alone. Moreover, FmlH specifically binds healthy human kidney tissue in a 29β-NAc–inhibitable manner, suggesting a key role for F9 pili in human kidney colonization. Thus, these glycoside antagonists of FmlH represent a rational antivirulence strategy for UPEC-mediated UTI treatment.

urinary tract infection | glycomimetics | structure-based drug design | host–pathogen interactions | antibiotic-sparing therapeutic

Urinary tract infections (UTIs) are one of the most prevalent infections, afflicting 15 million women per year in the United States alone, with annual healthcare costs exceeding $2 to $3 billion (1–3). Nearly 50% of women will experience at least one UTI in their lifetime. Despite appropriate and often successful clearance of bacteriuria by antibiotic treatment, 20% to 30% of women will experience a recurrence within 6 mo of the initial acute UTI (1, 4). Kidney infection, or pyelonephritis, represents a severe manifestation of UTI, with ∼250,000 cases and 100,000 hospitalizations per year in the United States (5). Acute pyelonephritis requires hospital admission and i.v. antibiotics to thwart the long-term sequelae of kidney failure and renal scarring, and, together with bacteremia, results in a mortality rate of 10% to 20% (6–8). With the global dissemination and increase of antibiotic resistance, treatment of UTI is becoming a serious clinical challenge (9). Antibiotic susceptibility tests indicate that many uropathogens are resistant to traditional first-line antibiotics like trimethoprim-sulfamethoxazole (TMP-SMZ) and even to last-line antibiotics such as ciprofloxacin and colistin (10–15). The diminishing efficacy of antibiotic therapies toward UTIs and other infectious diseases demands alternative antibiotic-sparing approaches to combat bacterial pathogens. Recently, promising efforts have been made to target the virulence mechanisms that cause bacterial infection. These studies have provided much-needed therapeutic alternatives, which simultaneously reduce the burden of antibiotic resistance and minimize disruption of gastrointestinal microbial communities that are beneficial to human health (16).

Uropathogenic *Escherichia coli* (UPEC) is the main etiological agent of UTIs, accounting for greater than 80% of community-acquired UTIs (17, 18). Comparative genomic studies have revealed that UPEC strains are remarkably diverse, such that only 60% of the genome is shared among all strains (19). As a consequence, UTI risk

Significance

The emergence of multidrug-resistant bacteria, including uropathogenic *Escherichia coli* (UPEC), makes the development of targeted antivirulence therapeutics a critical focus of research. During urinary tract infections (UTIs), UPEC uses chaperone–usher pathway pili tipped with an array of adhesins that recognize distinct receptors with sterochemical specificity to facilitate persistence in various tissues and habitats. We used an interdisciplinary approach driven by structural biology and synthetic glycoside chemistry to design and optimize glycomimetic inhibitors of the UPEC adhesin FmlH. These inhibitors competitively blocked FmlH in vitro, in in vivo mouse UTI models, and in ex vivo healthy human kidney tissue. This work demonstrates the utility of structure-driven drug design in the effort to develop antivirulence therapeutic compounds.

Author contributions: V.K., M.E.H., A.R.M., J.S.P., J.W.J., and S.J.H. designed research; V.K. and J.W.J. designed compounds; V.K., M.E.H., A.R.M., R.C., J.S.P., and L.K.M.-M. performed research; A.R.M., R.C., and L.K.M.-M. synthesized compounds; V.K., M.S.C., and J.S.P. purified proteins; V.K. and J.S.P. performed virtual screening, X-ray crystallography, ELISA, bio-layer interferometry, and immunofluorescence experiments; M.E.H. performed animal experiments; V.K., A.R.M., R.C., J.S.P., L.K.M.-M., and M.S.C. contributed new reagents/analytic tools; V.K., M.E.H., A.R.M., J.S.P., J.W.J., and S.J.H. analyzed data; V.K., M.E.H., J.S.P., J.W.J., and S.J.H. interpreted all data; and V.K., M.E.H., A.R.M., J.W.J., and S.J.H. wrote the paper.

Conflict of interest statement: J.W.J. and S.J.H. are inventors on US patent US8937167 B2, which covers the use of mannoside-based FimH ligand antagonists for the treatment of disease. J.W.J., M.E.H., and S.J.H. have ownership interests in Fimbrion Therapeutics and may benefit if the company is successful in marketing mannosides.

This article is a PNAS Direct Submission.

Data deposition: The atomic coordinates and structure factors have been deposited in the Protein Data Bank, www.wwpdb.org (PDB ID codes 6AOW, 6AOX, 6AOY, 6ARM, 6ARN, 6ARO, and 6AS8).

[1]To whom correspondence may be addressed. Email: janetkaj@wustl.edu or hultgren@wustl.edu.

This article contains supporting information online at www.pnas.org/lookup/suppl/doi:10.1073/pnas.1720140115/-/DCSupplemental.

Published online March 5, 2018.

and outcome are determined by complex interactions between host susceptibility and diverse bacterial urovirulence potentials, which can be driven by differences in the expression and regulation of conserved functions. The ability of UPEC to colonize various habitats, such as the gut, kidney, and bladder, depends in large part on the repertoire of adhesins encoded in their genome. The most common mechanism for adhesion utilized by UPEC is mediated through the chaperone–usher pathway (CUP), which generates extracellular fibers termed pili that can confer bacterial adhesion to host and environmental surfaces, facilitate invasion into host tissues, and promote interaction with other bacteria to form biofilms (20). Phylogenetic analysis of *Escherichia* genomes and plasmids predicts at least 38 distinct CUP pilus types, with single organisms capable of maintaining as many as 16 distinct CUP operons (21). Many of these CUP pilus operons contain two-domain, tip-localized adhesins, each of which likely recognize specific ligands or receptors to mediate colonization of a host and/or environmental niche. For example, the type 1 pilus adhesin FimH binds mannosylated glycoproteins on the surface of the bladder epithelium, which is crucial for the establishment of cystitis (22, 23). The structural basis of mannose (Man) recognition by the N-terminal–receptor binding domain, or lectin domain (LD), of FimH has been leveraged to rationally develop high-affinity aryl mannosides (24–32). In mouse models of UTI, we have previously demonstrated that orally bioavailable mannosides that tightly bind FimH can prevent acute UTI, treat chronic UTI, and potentiate the efficacy of existing antibiotic treatments like TMP-SMZ, even against antibiotic-resistant *E. coli* strains (28). Thus, use of mannosides that target the adhesin FimH represents the first successful application of an antivirulence strategy in the treatment of UTI.

A homolog of the type 1 pilus, the F9 pilus, is one of the most common CUP pili in the *E. coli* pan genome and an important urovirulence factor employed by UPEC for the maintenance of UTI (21, 33). Our recent work has demonstrated that UPEC upregulates the expression of F9 pili in response to bladder inflammation and epithelial remodeling induced upon UPEC infection (34). These pili display the FimH-like adhesin FmlH, which is capable of binding terminal galactose (Gal), *N*-acetylgalactosamine (GalNAc), or Thomsen-Friedenreich antigen (TF) [Gal(β1-3)GalNAc(α)]. FmlH was shown to bind TF within naïve or infected kidneys and to Thomsen nouvelle antigen (Tn) (GalNAc) within the inflamed bladder epithelium during chronic, unresolved UTI. Deletion of FmlH in the urosepsis isolate CFT073 resulted in a competitive defect in the ability of this strain to maintain murine UTI in C3H/HeN female mice. Furthermore, vaccination with the LD of FmlH ($FmlH_{LD}$) as the challenge antigen significantly protected mice from developing UTI. Thus, we have shown that FmlH serves a key role in the UPEC pathogenesis cascade and represents a promising target for antivirulence therapies for UTI in both the bladder and kidney habitats.

Herein, we describe the discovery and structure-based optimization of high-affinity aryl galactoside and *N*-acetylgalactosaminoside FmlH ligands that potently inhibit the function of FmlH. Treatment with these FmlH antagonists significantly reduced bacterial burdens in the kidneys and bladders of infected mice, thereby demonstrating promising translational value in the treatment of UTI in humans. The results of these studies, together with our previous work on FimH mannosides, further support the mechanistic and therapeutic value of antivirulence strategies that leverage structure-function relationships of diverse bacterial adhesins for the rational design of high-affinity glycosides for the treatment of UTI and other bacterial infections.

Results

***O*-nitrophenyl β-Galactoside Identified as Early Lead Inhibitor of the F9 Pilus Adhesin FmlH.** We revealed in a previous communication that FmlH binds surface glycan receptors containing terminal Gal, GalNAc, or TF residues (34). Given the role of FmlH in UTI pathogenesis, we aimed to develop high-affinity galactoside antagonists of FmlH through an X-ray structure-guided medicinal chemistry approach. This strategy entailed (*i*) screening a select library of galactosides through multiplex ELISA arrays for initial lead compund identification; (*ii*) an iterative process of cocrystal structure determination, virtual screening, structure-based ligand design, and in vitro biochemical characterization; and (*iii*) evaluation of the top lead compound in a mouse model of UTI (Fig. 1*A*). Toward these goals, we first investigated whether Gal, GalNAc, and TF could be adapted to function as soluble, competitive inhibitors of FmlH. To that end, an ELISA-based competition assay was developed to detect binding of $FmlH_{LD}$ to surface-immobilized desialylated bovine submaxillary mucin (ds-BSM) in the presence or absence of soluble compounds (Fig. 1*A*). As expected, Gal, GalNAc, and TF were each capable of inhibiting $FmlH_{LD}$ at a concentration of 1 mM, with GalNAc exerting greater inhibitory potency than TF or Gal. However, neither Man nor glucose (Glc) had any detectable effect on the ability of $FmlH_{LD}$ to bind ds-BSM (Fig. 1*B*). Lactose (Lac), or Gal(β1-4)Glc, was also incapable of inhibiting $FmlH_{LD}$, demonstrating the high selectivity in which $FmlH_{LD}$ engages Gal-containing glycans (Fig. 1*B*). *O*-nitrophenyl β-galactoside (ONPG) and isopropyl β-thiogalactoside (IPTG) were also tested for inhibition in this exploratory phase of our search for FmlH inhibitors. While IPTG exerted minor inhibitory activity at 100 μM, ONPG was found to block $FmlH_{LD}$ from interacting with ds-BSM more effectively than Gal, GalNAc, or TF (Fig. 1*B*). The strong inhibitory potency of ONPG suggested that β-galactosides could potentially be rationally designed with higher affinity by specifically targeting residues within and surrounding the sugar binding pocket of FmlH.

Therefore, X-ray crystallography was implemented to elucidate the 3D structures of both apo and ligand-bound $FmlH_{LD}$ (*SI Appendix*, Table S1). First, a crystal structure of apo $FmlH_{LD}$ was solved at 1.6 Å resolution by molecular replacement using $FimH_{LD}$ [Protein Data Bank (PDB) ID 3MCY] as the search model. Within this structure, two copies of $FmlH_{LD}$ are found in the asymmetric unit, each of which adopts a canonical β-sandwich fold, with three distinct binding loops (loop 1: residues 10 to 15; loop 2: residues 44 to 53; and loop 3: residues 132 to 142) that form a wide, shallow, solvent-exposed binding pocket (Fig. 1 *C* and *D*). Within the binding pocket of both copies resides a sulfate ion, which interacts with residues implicated in Gal binding (Fig. 1*D*). Cocrystal structures of $FmlH_{LD}$ bound to TF and of $FmlH_{LD}$ bound to ONPG were also solved to 2.1 Å and 1.8 Å, respectively. Structural overlay of the apo and ligated crystal structures yields root-mean-square deviation (RMSD) values that fall within 0.6 Å, suggesting that $FmlH_{LD}$ generally adopts the same active or functional conformational state in the absence or presence of ligand (Fig. 1*C*). This functional conformational state most likely corresponds to a high-affinity conformation of FmlH, as the $FmlH_{LD}$ structures exhibit a higher degree of structural homology to the high-affinity conformation of FimH (RMSD values of 0.8 to 0.9 Å) than to the low-affinity conformation of FimH (RMSD values of 1.7 to 1.9 Å) (34–38).

The cocrystal structure of $FmlH_{LD}$-TF reveals two copies of $FmlH_{LD}$-TF in the unit cell, in which each TF adopts a distinct ligand conformation (Fig. 1*D*). In both copies, the terminal Gal in TF occupies the cleft of the binding pocket through direct polar interactions with residues F1, D53, K132, and N140. In contrast, the orientation of the GalNAc in TF differs significantly between the two copies of FmlH. In chain A, the GalNAc sugar points toward loop 3, with the carbonyl group of GalNAc forming a hydrogen bond (H-bond) with the guanidinium group of R142. In chain B, however, the GalNAc packs against and forms a H-bond with the hydroxyl group of Y46. Accordingly, the differences in the orientation of bound ligand across the two copies are accompanied by slight differences in orientation of the side chains of the interacting residues Y46 and R142. The multiple binding modes observed for a single ligand suggests that the

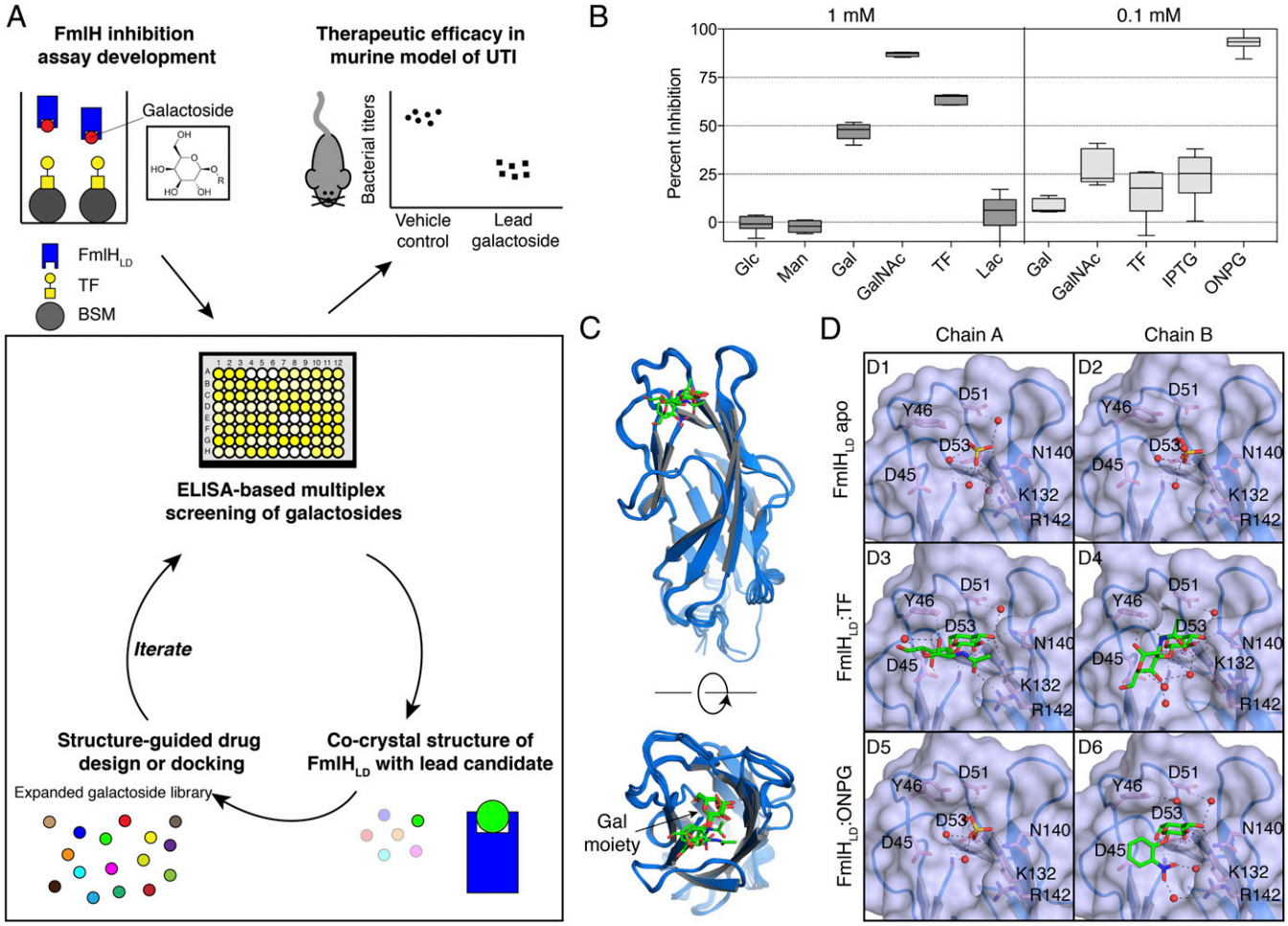

Fig. 1. Biochemical and structural characterization of early galactoside antagonists of FmlH. (*A*) Strategy for structure-guided drug design and evaluation of FmlH-targeting galactosides. A select library of galactosides were initially assessed in an ELISA-based competition assay for inhibition of FmlH binding to sialidase-treated BSM, with BSM indicated by gray circles, TF residues indicated by the yellow square-circle conjugates, biotinylated FmlH$_{LD}$ by blue rectangles, and galactosides shown as colored circles. Cocrystal structures of FmlH$_{LD}$ bound to a lead compound facilitated virtual screening and structure-guided drug design for biochemical evaluation of an expanded galactoside library. The top lead compound would then be tested as a treatment in a mouse model of UTI. (*B*) ELISA-based competition assay performed in triplicate in the absence or presence of 1 mM or 0.1 mM compounds with at least two biological replicates. Data are reported as the mean percent inhibition, with the box indicating the 25th to 75th percentiles and the whiskers indicating the 2.5th and 97.5th percentiles. (*C*) Structural alignment of FmlH$_{LD}$ from an apo FmlH$_{LD}$ crystal structure (PDB ID 6AOW), a FmlH$_{LD}$-TF cocrystal structure (PDB ID 6AOX), and a FmlH$_{LD}$-ONPG cocrystal structure (PDB ID 6AOY). (*D*) Crystal structures of sulfate ions or ligands bound in the FmlH$_{LD}$ binding pocket, with H-bonding (black dashed lines) indicated between sulfate ions (yellow sticks), ligands (green sticks), water molecules (red spheres), or side chains (pink sticks).

wide, shallow nature of the Gal binding pocket in FmlH would enable galactosides to possibly bind FmlH with diverse interactions and conformations.

The FmlH$_{LD}$-ONPG cocrystal structure also shows two copies of FmlH$_{LD}$ in the unit cell, in which a sulfate ion occupies the binding pocket of chain A while ONPG occupies the binding pocket of chain B (Fig. 1*D*). As expected, the Gal component of ONPG resides in the cleft of the binding pocket, while the solvent-exposed nitrophenyl group mediates a polar or salt-bridge interaction with R142 through an intricate network of H-bonds with water molecules. Furthermore, the positioning of the Gal component of ONPG aligns with that of the Gal residue of TF (Fig. 1*C*). Moreover, the conformation of the FmlH binding pocket observed in this FmlH$_{LD}$-ONPG cocrystal structure resembles the binding pocket conformation in the FmlH$_{LD}$-TF cocrystal structure, reflecting a high-affinity binding orientation that can be targeted for drug discovery. These results and observations strongly suggested that the FmlH$_{LD}$-ONPG cocrystal structure represents an appropriate structural candidate for use in virtual screening to aid in the design of galactoside compounds specific for FmlH.

Virtual Screen Identifies and Informs the Design of FmlH-Targeting Galactosides. An exhaustive virtual screen was performed using AutoDock Vina to computationally dock ∼1,800 known galactosides in the binding pocket of FmlH$_{LD}$ (from an FmlH$_{LD}$-ONPG cocrystal structure; PDB ID 6AOY), generating a ranked list of top binding poses and associated docking scores for each galactoside (*SI Appendix*, Fig. S1*A*). Top hits from the virtual screen were filtered according to group efficiency values and then visually inspected to aid and inform structure-guided drug design. In all cases, the Gal component of top-scoring galactosides bound to the cleft of the binding pocket, as expected. In addition, most of the high-scoring hits also interacted with specific hot-spot residues near the Gal binding pocket, which we sought to leverage for compound optimization. These hot-spot residues included (*i*) residue Y46, which caps the top of the binding pocket and can contribute hydrophobic interactions; (*ii*) residue K132, which lies at the bottom of the sugar binding pocket and can engage polar groups linked to the Gal sugar; and (*iii*) residue R142, which points toward an empty, solvent-exposed cleft near the binding pocket and can contribute electrostatic interactions (*SI Appendix*, Fig. S1*B*). These visual

insights were then considered in our rational design strategy for FmlH-targeting galactoside antagonists.

Design and Synthesis of FmlH-Targeting Galactoside Antagonists. To increase FmlH binding affinity and explore structure-activity relationships (SARs), we constructed a large library of galactoside analogs (Fig. 2). Based on the docking results, we predicted that β-Gal isomers would be preferred over α-Gal and that *ortho* positioning of functional groups on a phenyl scaffold would best facilitate interactions with specific sites within the binding pocket, namely hot-spot residues Y46 and R142. Accordingly, we synthesized and evaluated small sets of phenyl galactosides with *ortho*-substituted functional groups (**2** to **6**; Fig. 2*A*). We also either purchased or synthesized several other phenyl galactosides, which contained *meta* or *para* substituents on the aglycone ring (**7** to **11**; Fig. 2*A*), and other aryl and heterocyclic galactosides (**12** to **22**; Fig. 2 *B* and *C*). This allowed us to derive meaningful SARs for informing further design and optimization of improved galactosides. In addition, we tested natural-product galactosides isolated from cranberries and other natural sources (**23** to **27**; Fig. 2*D*). The promising activity of the simple galactoside ONPG (**4β**) in the initial screen, coupled with the hot-spot residues identified in virtual screening, prompted us to expand our FmlH-ligand design strategy with a compound series containing biphenyl aglycones (**28** to **32**; Fig. 2*E*), such as **29β-NAc**, the *N*-acetyl-β-galactosaminoside with an *m*-carboxylic acid on the B-ring designed to directly interact with the hot-spot residue R142 (*SI Appendix*, Fig. S1 *B* and *C*). To confirm the predicted preference for the β-Gal isomers, we also synthesized and tested many corresponding α-Gal isomers. Compounds were synthesized by using one of two general synthetic glycosylation methods involving either a reaction between Gal pentaacetate and phenols promoted by boron trifluoride or a Koenigs–Knorr-type reaction of galactosyl halide with aryl alcohols (*SI Appendix*, Fig. S2).

Biochemical Characterization of FmlH Antagonists. Selected top-hit glycosides and a few low-scoring analogs from the virtual screen, as well as synthetic galactosides, were tested in the ELISA-based competition assay for their ability to inhibit binding of $FmlH_{LD}$ to ds-BSM. Direct comparison of inhibitory potency among galactosides led to delineation of basic SARs (Fig. 3 *A*–*C* and *SI Appendix*, Table S2). When tested at 100 μM, the phenyl β-galactoside **1β** (beta isomer of **1**; Fig. 2*A*) exhibited significantly higher binding inhibition (77%) than Gal (8.1%), indicating that the phenyl group significantly enhances binding to $FmlH_{LD}$ (Fig. 3*A*). Various *ortho* substituents on the phenyl ring additionally conferred substantial improvements in inhibitory potency, as observed with **2β** (87%), **3β** (95%), **4β** (ONPG; 93%), **5β** (97%), and **6β** (90%). In contrast, the *meta*-methoxy groups in compound **7β** (76%) did not enhance binding strength compared with **1β**. Further, *para*-substituted functional groups displayed variable inhibitory potencies relative to **1β**, with enhancements observed in **8β** (86%) and **9β** (86%), with no significant effect observed in **11β** (78%) or **11β-thio** (72%), and with a reduction observed in **10β** (65%). Thus, we deduced that the *ortho*-substituted phenyl β-galactosides generally outperformed other simple phenyl galactosides.

Complex heterocyclic galactosides, such as coumarins **12β** (85%) and **14β** (89%), which differ only by a methyl group, displayed significant inhibitory potencies against $FmlH_{LD}$, while the related galactoside **13β** (50%) displayed reduced inhibitory activity, likely because of its fluoro substituents (Fig. 3*A* and *SI Appendix*, Table S2). Resorufin galactoside **15β** (80%) also showed similar potency compared with the phenyl β-galactoside **1β**. These combined results suggest that the substituents of **12β** are responsible for augmenting affinity relative to **1β**. In contrast, indoles **16β** (22%) and 17**β** (41%) performed poorly as inhibitors of $FmlH_{LD}$. Naphthyl galactosides **18β** (46%) and **19β** (79%), in addition to isoquinoline **21β** (15%), showed no improvement in activity relative to **1β**. However,

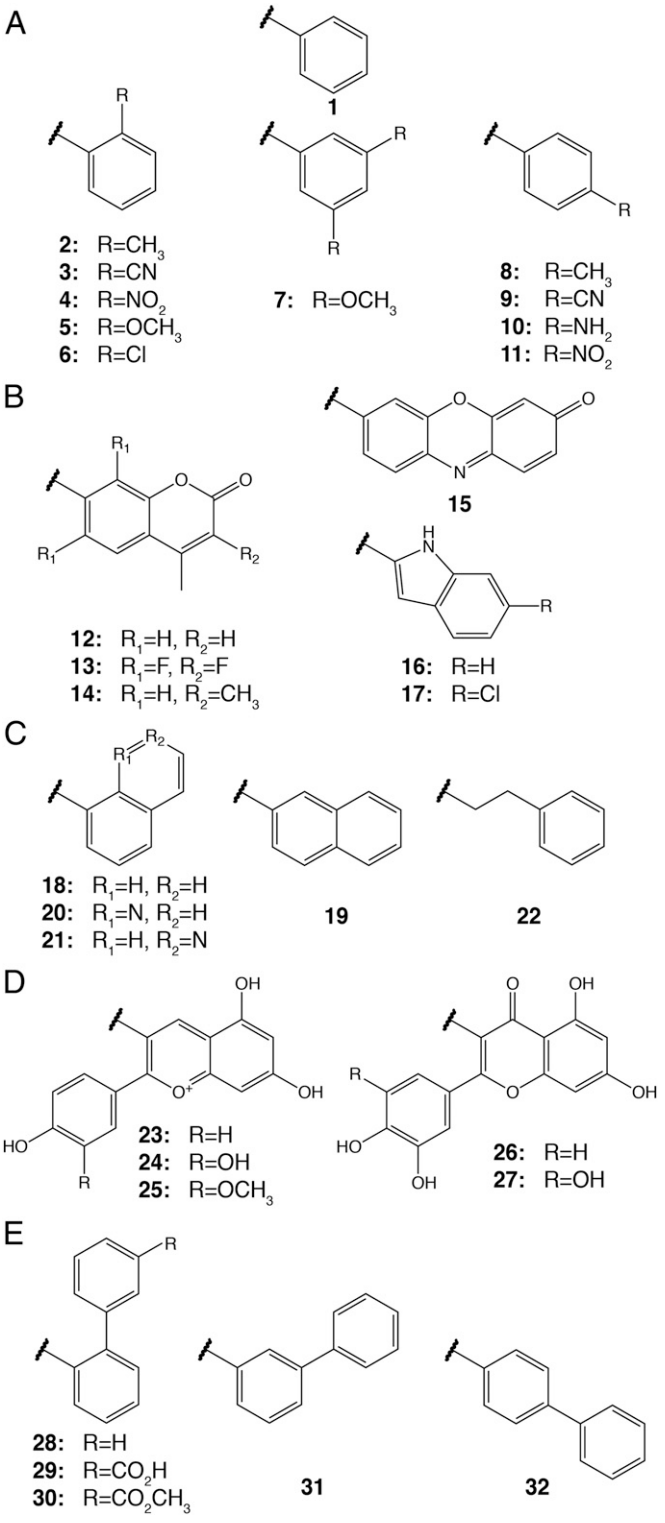

Fig. 2. Grouped organization of galactosides evaluated for $FmlH_{LD}$ inhibition. The major groups include the phenyl (*A*), heterocyclic (*B*), napthyl/quinoline/phenylethyl (*C*), natural product (*D*), and biphenyl (*E*) series.

quinoline **20β** (95%) displayed significantly higher inhibition than **1β** and **18β**. This advocates that the electron pair-donating nitrogen atom in **20β** is making a specific interaction with FmlH. This observation is consistent with the pattern of SARs, indicating that the *ortho* position is key to enhancing inhibitory potency against $FmlH_{LD}$.

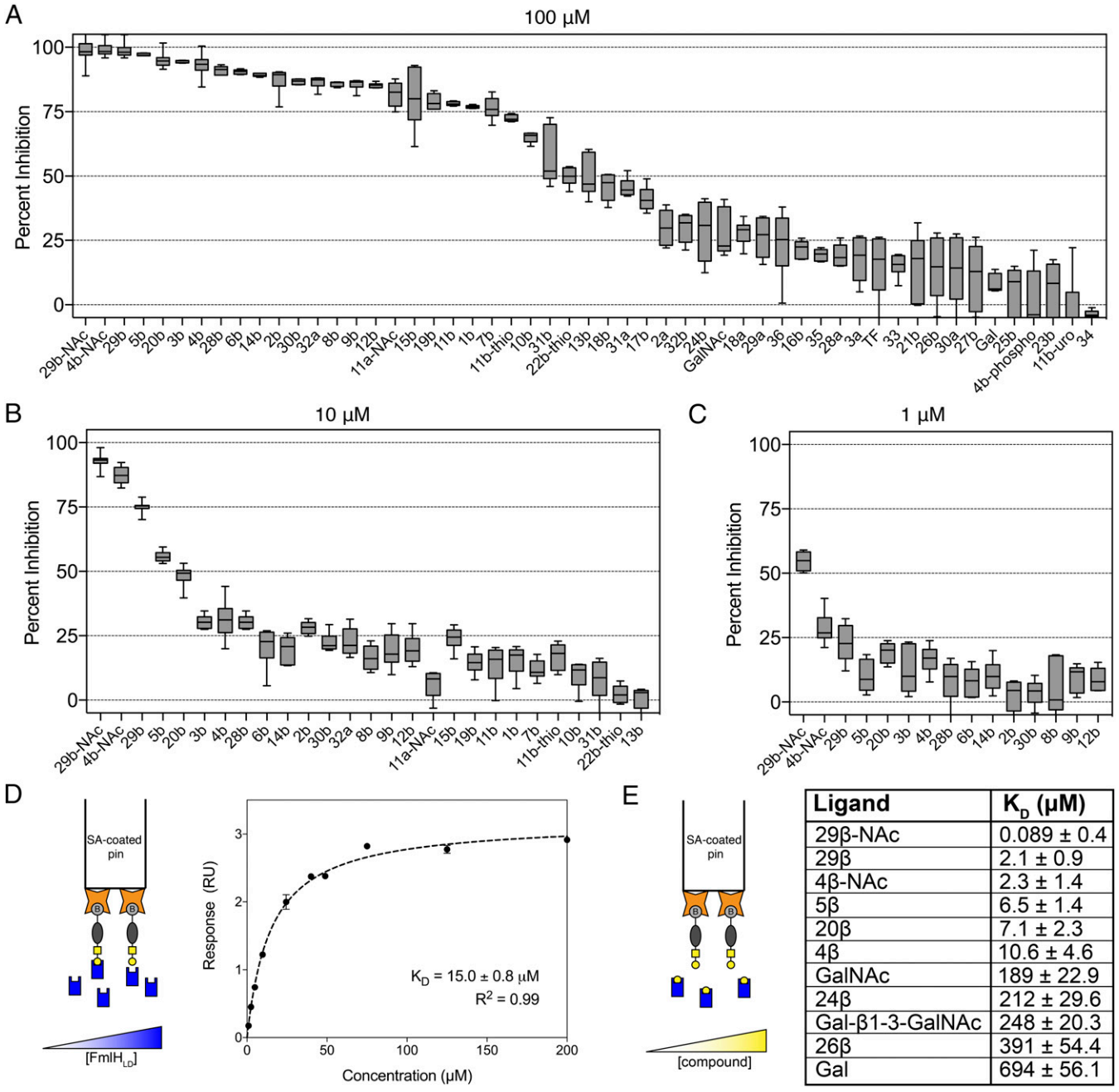

Ligand	K_D (μM)
29β-NAc	0.089 ± 0.4
29β	2.1 ± 0.9
4β-NAc	2.3 ± 1.4
5β	6.5 ± 1.4
20β	7.1 ± 2.3
4β	10.6 ± 4.6
GalNAc	189 ± 22.9
24β	212 ± 29.6
Gal-β1-3-GalNAc	248 ± 20.3
26β	391 ± 54.4
Gal	694 ± 56.1

Fig. 3. In vitro screening and affinity determination of galactosides against FmlH$_{LD}$. (*A–C*) ELISA-based competition assay performed in triplicate in the absence or presence of (*A*) 100 μM, (*B*) 10 μM, and (*C*) 1 μM compounds with at least two biological replicates. Data are reported as the mean percent inhibition, with the box indicating the 25th to 75th percentiles and the whiskers indicating the 2.5th and 97.5th percentiles. a, α; b, β. (*D, Left*) Schematic of conventional BLI experiment, in which pins coated with streptavidin (orange stars) are loaded with biotinylated Ser-TF (gray ovals and yellow square-circle conjugates) and dipped into solutions of varying concentrations of FmlH$_{LD}$ (blue rectangles). (*Right*) Equilibrium analysis of soluble FmlH$_{LD}$ binding to immobilized Ser-TF according to a 1:1 binding model. (*E, Left*) Schematic of competitive BLI experiment, in which streptavidin-coated pins are dipped into a solution composed of a fixed concentration of FmlH$_{LD}$ in the presence of varying concentrations of galactoside (yellow circles). (*Right*) Equilibrium constants of soluble galactoside-mediated inhibition of FmlH$_{LD}$ in binding immobilized Ser-TF in accord with $R^2 > 0.85$.

We also evaluated naturally occurring galactosides derived from cranberries and other natural sources in this screen (Fig. 3*A* and *SI Appendix*, Table S2). These compounds included anthocyanidin (pelargonidin, **23β**; cyanidin, **24β**; peonidin, **25β**) and flavonol (quercetin, **26β**; myricetin, **27β**) β-galactosides. Generally, these compounds exhibited moderate to weak inhibition of FmlH$_{LD}$ binding, with little enhancement in inhibition relative to Gal (8.1%). The only significant binders were **24β** (29%) and **26β** (14%). Comparison of the anthocyanidin family indicates that the 3′ or *meta*-substituted hydroxyl group on the B-ring of **24β** is critical for its specific interaction with FmlH. Absence of this *meta* substituent in **23β** (0.7%) or methylation of the hydroxyl group in **25β** (3.6%) abrogates potency, suggesting that the hydroxyl group of **24β** might participate in a H-bond to a specific residue in the FmlH$_{LD}$ binding pocket. Additional inhibitory screens performed with cranberry-derived compounds

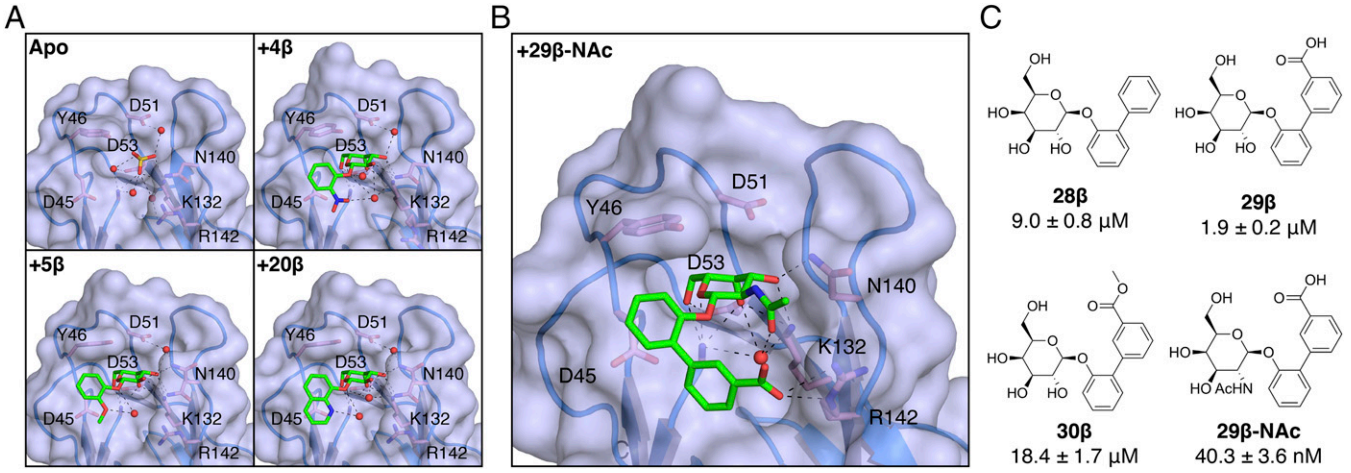

Fig. 4. Structural basis of galactoside inhibition of $FmlH_{LD}$. (*A*) Crystal structures of sulfate ions or galactosides bound in the $FmlH_{LD}$ binding pocket, with H-bonding (black dashed lines) indicated between sulfate ions (yellow sticks), ligands (green sticks), water molecules (red spheres), or side chains (pink sticks). Crystal structures shown here include an apo $FmlH_{LD}$ crystal structure (PDB ID 6AOW), a $FmlH_{LD}$-**4β** cocrystal structure (PDB ID 6ARM), a $FmlH_{LD}$-**5β** cocrystal structure (PDB ID 6ARN), and a $FmlH_{LD}$-**20β** cocrystal structure (PDB ID 6ARO). (*B*) Cocrystal structure of **29β-NAc** bound to $FmlH_{LD}$ (PDB ID 6AS8). (*C*) SARs for **29β-NAc** and related compounds, with their corresponding IC_{50} values derived from the ELISA-based competition assay. IC_{50} values are reported for six replicates as the mean with SEM.

and fractions at 1 mM confirmed the specificity and necessity of the Gal sugar for inhibiting the binding pocket of FmlH (*SI Appendix*, Fig. S3 *A* and *B*).

Interestingly, the tested GalNAc-derived compounds possessed significantly higher inhibitory potency compared with their matched-pair Gal-derived counterparts, as exemplified with **4β-NAc** (87%) relative to **4β** (31%) when tested for inhibition at 10 μM (Fig. 3*B* and *SI Appendix*, Table S2). These results taught us that the N-acetyl group, together with other functional groups, contributes to binding by targeting distinct components of the binding pocket of FmlH. In contrast, the galactosides with α-linkages (**28α**-**30α**) or disaccharides with aglycone moieties (**33** to **35**) were generally poor inhibitors of FmlH, except for **11α-NAc** (82%) (Fig. 3*A* and *SI Appendix*, Table S2).

Consistent with the above-mentioned SARs, the *ortho* biphenyl galactoside **28β** (91%) was more potent than the *meta* **31β** (57%) or *para* **32β** (30%) analogs (Fig. 3*A* and *SI Appendix*, Table S2). Next, we installed a carboxylate group at the *meta* position on the biphenyl B-ring (**29β**), intended to target the pocket formed by N140 and R142, and found that **29β** exhibited greater inhibition (99%) compared with **28β** when tested at 100 μM. This pronounced difference in activity was further highlighted when these compounds were tested for inhibition at 10 μM and 1 μM (Fig. 3 *B* and *C* and *SI Appendix*, Table S2). Importantly, **30β** (87%), the methyl ester of **29β**, tested at 100 μM resulted in a reduction in binding, suggesting that the negative charge of the carboxylic acid likely mediates a critical electrostatic interaction with R142 of $FmlH_{LD}$. Lastly, we synthesized the GalNAc version of **29β** to increase its binding affinity and found that **29β-NAc** (93%) had significant improvement in activity over **29β** (75%) when tested at 10 μM. Final evaluation of the highest performing galactosides in the ELISA-based competition assay at concentrations of 10 μM and 1 μM allowed for a clearer ranking of compounds, where **29β-NAc** clearly stood out as the most potent (Fig. 3 *B* and *C* and *SI Appendix*, Table S2).

Determination of FmlH–Galactoside Binding Affinities. Bio-layer interferometry (BLI) was pursued to quantitate the binding affinity of the most promising FmlH antagonists. First, biotinylated serine-linked TF (Ser-TF) immobilized on streptavidin pins was incubated with varied titrations of $FmlH_{LD}$ in solution, and steady-state analysis of binding responses revealed a dissociation constant (K_d) of 15.0 ± 0.8 μM (Fig. 3*D*). Next, immobilized Ser-TF was incubated in solutions comprising a fixed concentration of $FmlH_{LD}$ but varying concentrations of galactosides to determine their inhibitory or dissociation constant (K_i or K_d) values (Fig. 3*E*). The BLI-based affinity determinations correlated well with the relative binding strengths measured in the ELISA-based competition assay (Fig. 3 *A*–*C* and *SI Appendix*, Table S2). The two lead compounds, **29β-NAc** and **29β**, bound tightly to $FmlH_{LD}$, with respective K_i values of ∼90 nM and 2.1 μM, which represent a ∼7,800-fold and ∼330-fold enhancement in binding affinity relative to Gal. Another promising compound, **4β-NAc**, bound $FmlH_{LD}$ with a K_i value of 2.3 μM. In summary, a combinatorial approach based on virtual /screening and structure-guided ligand design led to the discovery of small–molecular weight monomeric glycosides derived from Gal and GalNAc that function as effective antagonists of FmlH. Optimization of early hits to high-affinity *o*-biphenyl Gal and GalNAc antagonists was realized via *ortho* substitution on phenyl aglycones to facilitate interactions that significantly enhanced binding to FmlH.

Structural Basis of Galactoside Inhibition of FmlH. To elucidate the molecular basis for galactoside inhibition of FmlH, cocrystal structures of $FmlH_{LD}$ bound to **4β**, **5β**, **20β**, and **29β-NAc** were determined (Fig. 4 *A* and *B*). These galactosides share a common aglycone motif consisting of a phenyl ring with an *ortho*-substituted functional group. As predicted from computational studies, the sugar portion of all these galactosides resides within the cleft of the binding pocket. The phenyl groups directly attached to the sugar portion of all four compounds lie along the same 3D plane. In this nearly identical conformation, the phenyl ring is oriented perpendicularly to the side chain of residue Y46, revealing edge-to-face π-stacking, which likely contributes to the affinity enhancement observed for all β-galactosides. For **4β**, **5β**, and **20β**, the *ortho* substituents point toward R142 but are too distant (>7 Å) for direct interaction and, instead, form H-bonds with water molecules that, in turn, interact with residues K132 and R142 (Fig. 4*A*). Thus, we deduced that the marked affinity enhancement observed for **4β**, **5β**, and **20β** is due to a combination of (*i*) indirect interactions between the *ortho* substituent and residues K132 and R142 formed by an intricate network of water-mediated H-bonds and (*ii*) edge-to-face π-stacking between the phenyl ring and residue Y46.

In contrast to simple phenyl galactosides, the biphenyl scaffold of **29β-NAc** presents the carboxylic acid to engage in a direct

charge–charge interaction with the guanidinium side chain of R142 (Fig. 4*B*). The lower potency of the methyl ester derivative **30β** is further evidence that the charge–charge interaction likely drives the observed affinity enhancement (Fig. 4*C*). The improved affinity of **29β-NAc** relative to **29β** is also due to additional interactions mediated by the N-acetyl group in H-bonding to a water molecule captured by the biphenyl aglycone and the side chain of residue K132 (Fig. 4 *B* and *C*). Altogether, analysis of all X-ray crystal structures of ligand-bound FmlH offers two general mechanisms for the significant enhancement in binding affinity of galactosides relative to Gal: edge-to-face π-stacking with Y46 and polar or electrostatic charge–charge interactions with K132 and R142.

FmlH Antagonist Effectively Treats Murine UTI in Vivo and Prevents Binding to Human Kidney Tissue. We previously reported that FmlH binds to naïve kidney and inflamed bladder tissue and plays a critical role in chronic UTI, as abrogation of its function through genetic deletion or vaccination results in significant attenuation in the ability of UPEC to cause chronic UTI (34). Thus, we hypothesized that galactosides that inhibit the function of FmlH would have efficacy in the treatment and/or prevention of UTI. To assess therapeutic potential, the lead compound **29β-NAc** was evaluated for its ability to reduce bacterial burdens in the urinary tracts of C3H/HeN mice during chronic UTI. We previously defined chronic cystitis in C3H/HeN mice as urine titers of $>10^4$ CFU/mL lasting at least 2 to 4 wk, as well as bladder inflammation and edema at euthanasia (39). Further, C3H/HeN mice are genetically predisposed to vesicoureteral reflux (retrograde flow of urine from the bladder to the kidneys), which can lead to bacterial colonization of the kidneys, renal abscess formation, scarring, and atrophy (40). Accordingly, we observed high levels of kidney colonization by CFT073 in control (vehicle-treated) animals. When delivered intravesically, **29β-NAc** significantly reduced bacterial burdens in both the bladder and the kidneys of these mice (Fig. 5 *A* and *B*). For comparison, mannoside 4Z269, which inhibits the type 1 pilus adhesin FimH, also significantly reduces titers of CFT073 from the bladders and kidneys of infected mice relative to vehicle control (Fig. 5 *A* and *B*). When administered together, **29β-NAc** and 4Z269 eradicated bacteria from the kidney in nearly all mice while also reducing bacterial titers in the bladder, suggesting that FimH mannosides and FmlH galactosides may function synergistically to target distinct bacterial adhesins or communities within the kidney habitat (Fig. 5 *A* and *B*).

To show relevance to human UTI, we assessed FmlH and FmlH-targeting galactosides through immunofluorescence analysis of $FmlH_{LD}$ binding to human kidney and bladder biopsied tissue determined to be nonmalignant. While $FmlH_{LD}$ does not appear to bind to healthy human bladder tissue, $FmlH_{LD}$ does bind to healthy human kidney tissue, particularly in regions resembling the collecting ducts and distal tubules of the kidney (Fig. 5*C* and *SI Appendix*, Figs. S4 and S5). As a negative control, the binding null mutant $FmlH_{LD}$ K132Q, which lacks the ability to bind ds-BSM in vitro (*SI Appendix*, Fig. S6), was incapable of binding kidney tissue, suggesting that $FmlH_{LD}$ specifically recognizes receptors naturally present in human kidney tissue (Fig. 5*C*). These observations are consistent with the previously reported binding phenotypes in mice, in which FmlH can bind naïve mouse kidney tissue, but not naïve mouse bladder tissue, and can bind to receptors in inflamed bladder tissue (34). Moreover, incubation of **29β-NAc** with $FmlH_{LD}$ prevented binding to human kidney tissue, suggesting that these results may translate to humans. Importantly, these collective data provide substantial evidence that aryl glycoside–based FmlH antagonists derived from β-Gal or β-GalNAc can serve as an effective therapy for persistent UTIs, including pyelonephritis, for which there is an enormous unmet medical need.

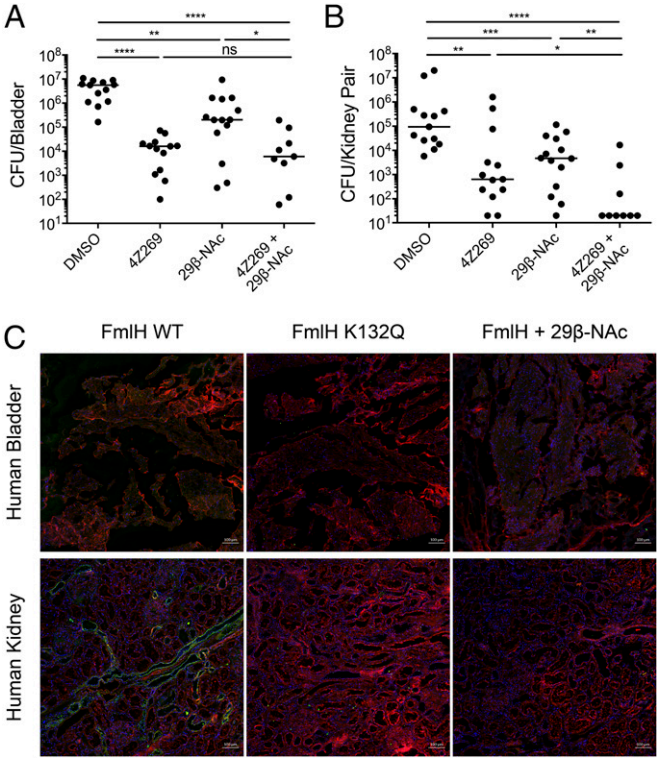

Fig. 5. Evaluation of galactosides for treatment of UTI and relevance in humans. (*A* and *B*) Bacterial titers in bladders (*A*) or kidneys (*B*) from C3H/HeN mice experiencing chronic cystitis transurethrally inoculated with 10% DMSO (three replicates, $n = 13$), or 50 mg/kg of 4Z269 (three replicates, $n = 13$), of **29β-NAc** (three replicates, $n = 14$), or of both 4Z269 and **29β-NAc** (two replicates, $n = 9$). Bars indicate median values. $^*P < 0.05$, $^{**}P < 0.01$, $^{***}P < 0.001$, $^{****}P < 0.0001$; ns, not significant; two-tailed Mann–Whitney *U* test. (*C*) Immunofluorescence analysis of $FmlH_{LD}$ WT, $FmlH_{LD}$ K132Q, or $FmlH_{LD}$ WT in the presence of **29β-NAc** binding to human bladder or human kidney tissue. Green corresponds to FmlH, red corresponds to Wheat Germ Agglutinin, and blue corresponds to DAPI. Each image is representative of nine total images (three imaged areas of three tissue slices). (Scale bars: 100 μm.)

Discussion

UPEC is the causative agent of most UTIs, a common and very costly disease in women, children, and the elderly that is becoming increasingly resistant to antibiotic treatment. By leveraging our expertise in UPEC pathogenesis and structure-based drug design, we developed small-molecule Gal-based FmlH antagonists that show in vivo efficacy in the treatment of chronic UTI in mouse models. Virtual screening combined with rational design led to the identification of several naturally occurring cranberry and synthetic galactosides, the most potent of which binds FmlH with nanomolar affinity. X-ray crystallography revealed that potent galactosides achieve significant enhancements in binding affinity through interactions on opposite sides of the wide Gal binding pocket of FmlH. Appropriately substituted aryl groups, like those found in **4β/4β-NAc**, **5β**, and **20β**, are seen to mediate edge-to-face π-stacking interactions with Y46 of $FmlH_{LD}$. Further, the optimized biphenyl aglycone of compound **29β-NAc** contains an ideally positioned carboxyl group to mediate electrostatic interactions with R142 in addition to π-stacking interactions with Y46. Evaluation of the lead candidate **29β-NAc** in a mouse model of chronic UTI demonstrated significant reductions of bacterial burdens in the mouse kidney and bladder. Combination dosing with mannoside and galactoside resulted in near complete clearance of bacteria from the kidney and significant elimination of bacteria from the bladder. Furthermore, FmlH was shown to bind specifically to

human kidney tissue, which could be inhibited by **29β-NAc**. Additionally, FmlH has been shown to be up-regulated in urine samples directly isolated from human patients with UTI compared with expression during in vitro growth in media or normal urine (41), suggesting an important role for FmlH in human UTI. Thus, FmlH-targeting galactosides represent a rational antivirulence modality for the effective treatment of UPEC-mediated UTI.

Our rational strategy to discover receptor-mimicking galactosides targeting FmlH was similar to the strategy we followed for the development of FimH mannosides. However, the design of the galactoside and *N*-acetylgalactosaminoside antagonists of FmlH was met with distinct challenges. The most striking difference between FmlH and FimH is the binding affinity for their respective ligands: FimH binds soluble Man with a moderate binding affinity of ~5 to 10 μM, and FmlH binds soluble Gal with a weak binding affinity of ~700 μM (34, 42, 43). The weak binding affinity of FmlH, which is quite common for most carbohydrate–lectin interactions, rendered the development of high-affinity galactosides much more challenging. This disparity in affinity is a direct consequence of the substantial variance in the shape of the binding pocket. FimH binds Man with high affinity because of the deep, narrow pocket formed by loops 1, 2, and 3, in which loops 2 and 3 mediate specific polar interactions directly to Man and a water molecule and loop 1 serves as an affinity clamp to stymie dissociation of Man (35). In contrast, loop 1 in FmlH is more distant from loops 2 and 3 than it is in FimH and does not contribute to binding, which results in a widened, solvent-exposed pocket for weak Gal binding (Fig. 1*D*). In addition, the differences in binding pocket architecture dictate the sterically allowed linkage types. FimH has space at the tip of the LD between its parallel tyrosine gate (residues Y48 and Y137) to accept α-linked moieties, of which biaryl groups confer drastic enhancements in affinity through strong parallel face-to-face π-stacking interactions. In contrast, FmlH is capped at the very tip of the pocket with Y46, which biases specificity toward β-linked moieties, of which biaryl groups confer moderate enhancements in affinity through significant edge-to-face π-stacking interactions. Having accounted for these variations, our structure-guided medicinal chemistry approach, coupled with our in vivo work, has clearly demonstrated the future translational impact of galactosides as treatments for UTI.

It is noteworthy that our collective search for high-affinity antagonists of FmlH and FimH has led to discovery of biphenyl moieties as the preferred aglycone groups for high-affinity galactosides and mannosides, respectively. Pocket geometry dictates the type of biphenyl scaffold that is optimal. Thus, the best FimH-targeting mannosides contain *para* biphenyls in the alpha stereochemistry, while the best FmlH-targeting galactosides contain *ortho* biphenyls in the beta orientation. However, in both cases, H-bonding donors or acceptors on the B-ring result in significant enhancement in binding affinity through specific interactions outside the sugar binding pocket. Intriguingly, the inhibitory potency conferred by the *meta* carboxyl on the B-ring of **29β-NAc** is also appreciated in the significant inhibitory role of the *meta*-substituted group on the B-ring in cranberry compounds **24β** and **26β**, which suggests a common pharmacophore between our optimal synthetic compound and natural-product compounds in targeting FmlH. This study provides evidence that specific glycosidic compounds in cranberry can specifically bind and inhibit a bacterial adhesin. Furthermore, our work exposes a trend indicating that π-stacking of aromatic aglycones with binding pocket residues in the adhesin is essential in mimicking glycoprotein receptors and for developing tight-binding ligands in each lectin. Mimicking carbohydrates with small molecules is a long-sought-after goal in medicinal chemistry and chemical biology (44–46), and we believe that these results add significantly to this understanding and goal. This information can now be utilized not only in the future optimization of lead compound **29β-NAc** as a treatment for UTIs, but also in the rational design of numerous other lectin antagonists for the development of small-molecule glycoside-based drugs aimed at treating infections mediated by *E. coli* or other microbes (44).

The rapid increase and spread of antibiotic resistance, including multidrug-resistant forms of bacteria, has rendered many antibacterial therapies ineffective and threatens to undermine the biomedical strides made to promote human health and longevity (9). Selection pressures imposed by antibiotics on bacterial pathogens have promoted their proliferation, especially through overuse of antibiotics within the farming industry and inappropriate use or misuse among patients (47–50). Recent reports indicate that patients are now succumbing to bacterial strains which possess broad-spectrum resistance to all last-resort antibiotics, which many fear signals that antibiotic resistance will pave the way for the "next pandemic" (15). Antivirulence strategies that aim to reduce the pathogenicity of bacterial pathogens promise to provide the same therapeutic efficacy as antibiotics without introducing selective pressures that would promote widespread dissemination of resistance (16). Multiple antivirulence efforts will be required to combat the multiple mechanisms by which diverse bacterial pathogens colonize the host, which can include, for example, the targeting of CUP pilus adhesins or the biogenesis machinery responsible for the assembly of CUP pili (51). As highlighted in this work, UPEC employs an armament of diverse CUP pili to colonize and persist within changing local environments encountered during UTI pathogenesis, which suggests that targeting more than one CUP adhesin may indeed be a more effective strategy for combating UTIs. Herein, we have highlighted the overwhelming value of applying a deep mechanistic understanding of structure-function-virulence relationships of bacterial adhesins to the rational design of high-affinity carbohydrate glycomimetics for the treatment of UTI. This demonstration serves as a general model for the rational approach necessary to target virulence factors and disrupt their role in bacterial infections.

Materials and Methods

Ethics Statement. All animal experiments were conducted according to the National Institutes of Health (NIH) guidelines for housing and care of laboratory animals and performed in accordance with institutional regulations after pertinent review and approval by the Institutional Animal Care and Use Committee at Washington University School of Medicine (protocol 20150226). Deidentified human tissue was obtained from the Tissue Procurement Core at Washington University School of Medicine.

Protein Expression and Purification. FmlH residues 1 to 160 from UPEC strain UTI89 with a C-terminal six-histidine tag (i.e., $FmlH_{LD}$) were cloned into the IPTG-inducible plasmid pTrc99A. This construct was then transformed into and expressed in *E. coli* strain C600. Periplasms were isolated as previously described and dialyzed four times against PBS plus 250 mM NaCl (34). $FmlH_{LD}$ was purified from this periplasmic fraction by cobalt affinity chromatography through elution with 150 mM imidazole. $FmlH_{LD}$ was buffer exchanged into 10 mM Hepes [4-(2-hydroxyethyl)-1-piperazineethanesulfonic acid] (pH 7.5) and 50 mM NaCl, concentrated to 6 mg/mL, and stored stably at 4 °C for use in biochemical and biophysical assays.

In Silico Docking and Virtual Screening. Structure-based virtual screening through in silico docking was performed with AutoDock Vina (52). Existing Gal-based derivatives were identified through the ZINC12 database (53). Their 3D structures were extracted from the downloaded mol2 file as pdb coordinates and converted to pdbqt format using Open Babel (54). The crystal structure of apo FmlH was converted to its topology file using AutoDock Tools. The grid box was centered at the Gal binding pocket of FmlH, and its dimensions ($26 \times 26 \times 26$ Å^3) were chosen to accommodate bulky compounds and multiple potential binding modes at or near the binding pocket. The exhaustiveness of the search was set to a value of 15. The top binding modes and scores within this grid space were generated by AutoDock Vina. Custom in-house scripts in Bash and MATLAB were used to link these binding scores with compound properties such as molecular weight. Top binding modes were visualized in PyMOL.

Virtual screening of this library, which comprised galactosides ranging from 150 to 900 Da in molecular mass, yielded a mean docking score of

6.3 kcal/mol (1 kcal = 4.18 kJ), with a standard deviation of 0.73 kcal/mol and a range of 4 to 9 kcal/mol (*SI Appendix*, Fig. S1*A*). To prioritize hits, we abstained from directly comparing raw binding scores, as large, lipophilic molecules tend to have artificially high predicted binding interactions due to their contribution to hydrophobic interactions as calculated by the empirical scoring function of AutoDock Vina (52). Instead, the results of the virtual screen were evaluated per group efficiency (GE), which, in this context, measures the contribution of the aglycone group within each galactoside (indicated as X in the following equation) to the docking score (DS) with respect to the number of heavy atoms (HA) present in the aglycone group [$GE = (DS_X - DS_{Gal})/(HA_X - HA_{Gal})$]. Top hits were defined as galactosides with a GE value greater than 1.25 times the SD ($\sigma = 0.0016$ kcal/mol per HA) above the library mean ($\mu = 0.0011$ kcal/mol per HA), which constituted the top ∼10% of highest scoring galactosides (*SI Appendix*, Fig. S1*A*).

Synthesis of Galactosides and N-acetyl Aminogalactosides. Galactosides and N-acetyl aminogalactosides were synthesized by standard glycosylation chemistry, including boron trifluoride-mediated glycosidation and the Koenigs–Knorr reaction, respectively (*SI Appendix*, Fig. S2). In method A, boron trifloride-promoted glycosylation of phenols with Gal pentaacetate yielded corresponding acetylated aryl galactosides, which were treated with sodium methoxide in methanol to provide the corresponding aryl galactosides (**1β** to **3β**, **5β** to **9β**, **18β** to **19β**, and **28β** to **32β**; **2α** to **3α**, **18α** to **19α**, and **28α** to **32α**). In method B, final GalNAc and Gal analogs (**20β-NAc**, **21β**, **28β-NAc**, and **29β-NAc**) were synthesized from galactosyl halide and aryl alcohols via a Koenigs–Knorr-type reaction, which yielded aryl galactosides that were then deacetylated by treatment with methylamine in ethanol.

ELISA. Immulon 4HBX 96-well plates were coated overnight with 1 μg of bovine submaxillary mucin (Sigma). Coated wells were then treated with 100 μL of *Arthrobacter ureafaciens* sialidase (10 mU/mL) diluted in PBS for 1 h at 37 °C. Thereafter, wells were incubated with 200 μL of blocking buffer (PBS plus 1% BSA) for 2 h at 23 °C, followed by incubation with 100 μL of biotinylated $FmlH_{LD}$ diluted in blocking buffer to 20 μg/mL in the presence or absence of galactoside compounds for 1 h at 23 °C. After washing three times with PBS plus 0.05% TWEEN-20, 100 μL of streptavidin-HRP conjugate (BD Biosciences; 1:2,000 dilution in blocking buffer) was added to each well for 1 h at 23 °C. After a final round of washing, plates were developed with 100 μL of tetramethylbenzidine (BD Biosciences) substrate and quenched within 1 to 2 min with 50 μL of 1 M H_2SO_4, and absorbance was measured at 450 nm. This assay was used to determine percent inhibition values and inhibitory constant (IC_{50}) values where indicated.

BLI. Streptavidin pins were first dipped in a baseline in PBS (pH 7.4) for 120 s, followed by loading of 5 to 10 μg/mL biotinylated Ser-TF (Toronto Research Chemicals) in PBS for 300 s, quenching by 10 μg/mL biocytin in PBS for 240 s, and another baseline step in PBS for 120 s. Thereafter, pins were dipped in PBS for 120 s and transferred to protein samples (varying concentration of $FmlH_{LD}$ or fixed concentration of $FmlH_{LD}$ with varying concentration of galactoside compounds) for association for 300 to 600 s. Equilibrium binding response values were used to determine the affinity of interaction between $FmlH_{LD}$ and immobilized Ser-TF under a 1:1 binding model or between $FmlH_{LD}$ and galactosides in solution under a competitive one-site binding model.

Protein Crystallization and Structure Determination. Crystals of apo $FmlH_{LD}$ in 10 mM Hepes (pH 7.5) and 50 mM NaCl were grown by mixing 2 μL of protein (6 mg/mL) with 2 μL of mother liquor [0.2 M ammonium sulfate, 0.1 M NaCl, 0.1 M Mes [2-(*N*-morpholino)ethanesulfonic acid] (pH 5.6), and 28% PEG 3350] and equilibrated against 1 mL of mother liquor in the reservoir. Cocrystals of $FmlH_{LD}$ bound to TF or galactosides **4β** (in space group P 2 21 21), **5β**, and **20β** were grown by mixing 2 μL of protein (6 mg/mL) in the presence of 5 mM compound with 2 μL of mother liquor [0.2 M ammonium sulfate, 0.1 M NaCl, 0.1 M Mes (pH 5.6), and 32% PEG 3350] and equilibrated against 1 mL of mother liquor in the reservoir. These crystals were transferred into cryoprotectant [0.2 M ammonium sulfate, 0.1 M NaCl, 0.1 M Mes (pH 5.6), 35% PEG 4000, and 10% glycerol] and then flash frozen in liquid nitrogen. Cocrystals of $FmlH_{LD}$ bound to the galactoside **29β-NAc** were grown by mixing 2 μL of protein complex (10 mg/mL $FmlH_{LD}$ with a 1.2:1 molar ratio of **29β-NAc** to $FmlH_{LD}$) with 2 μL of mother liquor (0.7 M $LiSO_4$ and 2% PEG8000) and equilibrated against 1 mL of mother liquor in the reservoir. These crystals were transferred into cryoprotectant (1 M $LiSO_4$, 10% PEG8000, and 25% glycerol). Diffraction data for TF, **4β** (in space group C 1 2 1), and **29β-NAc** structures were collected at 100 K at an in-house facility equipped with a rotating anode Rigaku MicroMax 007 generator, a Rayonix Marmux X-ray source, and a Mar345 image plate detector. Diffraction data for apo, **4β**, **5β**, and **20β** structures were collected at 100 K at the ALS Beamline 4.2.2. Data were indexed and integrated in iMosflm (55), XDS (56), or HKL2000 and scaled by Scala (57). The phase problem was solved by molecular replacement using Phaser-MR in PHENIX (58) with $FimH_{LD}$ from PDB ID 3MCY. Several rounds of refinements were performed in PHENIX to improve the final models.

Mouse Infections. Seven- to 8-wk-old female C3H/HeN mice were obtained from Envigo. Mice were anesthetized and inoculated via transurethral catheterization with 50 μL of CFT073 bacterial suspension (∼1×10^8 to 2×10^8 CFU in total) in PBS. Mice experiencing high titers of bacteriuria (>10^4 CFU/mL) and edematous and inflamed bladders when killed after 2 wk, or chronic cystitis (39), were then transurethrally inoculated either with 50 mg/kg compound or vehicle control (10% DMSO). Mice were killed 6 h posttreatment, and bacteria colonizing the bladder or kidney were plated for quantification.

Immunofluorescence. Frozen, deidentified human bladder and kidney sections were obtained from the Tissue Procurement Core and stored stably at −80 °C. These tissue section slides were removed from the freezer and allowed to thaw at room temperature for 10 to 20 min. After applying a hydrophobic barrier pen around the tissue, slides were rehydrated in 200 μL buffer (5% BSA and 0.2% Triton X-100 in PBS) for 10 min. Buffer was gently aspirated and slides were blocked for 1 h at room temperature with 200 μL of buffer. Thereafter, buffer was gently aspirated and slides were incubated with 200 μL of sample overnight at 4 °C. Samples diluted in buffer included 50 μg/mL $FmlH_{LD}$ wild-type (WT), 50 μg/mL $FmlH_{LD}$ K132Q, and 50 μg/mL $FmlH_{LD}$ WT incubated with 100 μM **29β-NAc**. Samples were gently aspirated and slides were washed three times in buffer for 5 min each. Next, slides were incubated with our mouse anti-FmlH polyclonal antibody (1:500 dilution in buffer) for 1 h at room temperature. Slides were washed again three times in buffer and then incubated in the dark with donkey anti-mouse IgG Alexa Fluor 594 and Wheat Germ Agglutinin Alexa Fluor 633 (each 1:500 dilution in buffer) for 1 h at room temperature. Slides were washed once with buffer and then incubated in the dark with DAPI (1:1,000 dilution in buffer) for 5 min at room temperature. After washing twice with buffer, coverslips were mounted using 80 μL of mounting media. Slides were loaded onto a Zeiss LSM 880 Confocal Laser Scanning Microscope (Carl Zeiss, Inc.) equipped with a diode 405 to 430 laser, a HeNe 543 laser, and a HeNe 633 laser. Images were acquired with a 20×, 0.8 numerical aperture Zeiss Plan Apochromat objective using ZEN 2 imaging software.

Statistics. Mouse data are compiled from two (4Z269 plus **29β-NAc**) or three (all other treatments) independent experiments, with four or five mice per group per experiment. These data were analyzed using the uncorrected two-tailed Mann–Whitney *U* test in GraphPad Prisim v.5. ELISA data are reported as box-and-whisker plots indicating the mean, 2.5th, 25th, 75th, and 97.5th percentiles of at least two independent experiments, with three technical replicates per experiment.

ACKNOWLEDGMENTS. We thank members of the S.J.H. laboratory for helpful suggestions; Rick Stegeman at Washington University and Jay Nix at ALS Beamline 4.2.2 for technical assistance in X-ray data collection; and Wandy Beatty at Washington University for assistance and expertise in confocal microscopy. We thank Ocean Spray for their helpful advice and the Alvin J. Siteman Cancer Center at Washington University School of Medicine, the Barnes-Jewish Hospital, and the Institute of Clinical and Translational Sciences (ICTS) at Washington University in St. Louis, for the use of the Tissue Procurement Core, which provided human urinary tract tissue. The Alvin J. Siteman Cancer Center is supported, in part, by National Cancer Institute Cancer Center Support Grant P30 CA091842. The ICTS is funded by NIH National Center for Advancing Translational Sciences Clinical and Translational Science Award Program Grant UL1 TR002345. J.W.J. and S.J.H. were supported by NIH National Institute of Diabetes and Digestive and Kidney Diseases Grant R01 DK108840. V.K. was supported by Medical Scientist Training Program Grant T32GM07200.

1. Foxman B (2003) Epidemiology of urinary tract infections: Incidence, morbidity, and economic costs. *Dis Mon* 49:53–70.
2. Griebling TL (2005) Urologic diseases in America project: Trends in resource use for urinary tract infections in women. *J Urol* 173:1281–1287.
3. Gupta K, Hooton TM, Roberts PL, Stamm WE (2001) Patient-initiated treatment of uncomplicated recurrent urinary tract infections in young women. *Ann Intern Med* 135:9–16.
4. Foxman B (2010) The epidemiology of urinary tract infection. *Nat Rev Urol* 7:653–660.

5. Ramakrishnan K, Scheid DC (2005) Diagnosis and management of acute pyelonephritis in adults. *Am Fam Physician* 71:933–942.
6. Pertel PE, Haverstock D (2006) Risk factors for a poor outcome after therapy for acute pyelonephritis. *BJU Int* 98:141–147.
7. Efstathiou SP, et al. (2003) Acute pyelonephritis in adults: Prediction of mortality and failure of treatment. *Arch Intern Med* 163:1206–1212.
8. Roberts FJ, Geere IW, Coldman A (1991) A three-year study of positive blood cultures, with emphasis on prognosis. *Rev Infect Dis* 13:34–46.
9. WHO (2014) Antimicrobial resistance: Global report on surveillance 2014 (WHO, Geneva).
10. Guneysel O, Onur O, Erdede M, Denizbasi A (2009) Trimethoprim/sulfamethoxazole resistance in urinary tract infections. *J Emerg Med* 36:338–341.
11. Raz R, et al.; Israeli Urinary Tract Infection Group (2002) Empiric use of trimethoprim-sulfamethoxazole (TMP-SMX) in the treatment of women with uncomplicated urinary tract infections, in a geographical area with a high prevalence of TMP-SMX-resistant uropathogens. *Clin Infect Dis* 34:1165–1169.
12. Aypak C, Altunsoy A, Düzgün N (2009) Empiric antibiotic therapy in acute uncomplicated urinary tract infections and fluoroquinolone resistance: A prospective observational study. *Ann Clin Microbiol Antimicrob* 8:27.
13. Kallen AJ, Welch HG, Sirovich BE (2006) Current antibiotic therapy for isolated urinary tract infections in women. *Arch Intern Med* 166:635–639.
14. Karlowsky JA, Hoban DJ, Decorby MR, Laing NM, Zhanel GG (2006) Fluoroquinolone-resistant urinary isolates of *Escherichia coli* from outpatients are frequently multidrug resistant: Results from the North American Urinary Tract Infection Collaborative Alliance-Quinolone Resistance study. *Antimicrob Agents Chemother* 50:2251–2254.
15. McGann P, et al. (2016) *Escherichia coli* harboring mcr-1 and blaCTX-M on a novel IncF plasmid: First report of mcr-1 in the United States. *Antimicrob Agents Chemother* 60: 4420–4421.
16. Rasko DA, Sperandio V (2010) Anti-virulence strategies to combat bacteria-mediated disease. *Nat Rev Drug Discov* 9:117–128.
17. Ronald A (2003) The etiology of urinary tract infection: Traditional and emerging pathogens. *Dis Mon* 49:71–82.
18. Ronald AR, et al. (2001) Urinary tract infection in adults: Research priorities and strategies. *Int J Antimicrob Agents* 17:343–348.
19. Schreiber HL, 4th, et al. (2017) Bacterial virulence phenotypes of *Escherichia coli* and host susceptibility determine risk for urinary tract infections. *Sci Transl Med* 9: eaaf1283.
20. Waksman G, Hultgren SJ (2009) Structural biology of the chaperone-usher pathway of pilus biogenesis. *Nat Rev Microbiol* 7:765–774.
21. Wurpel DJ, Beatson SA, Totsika M, Petty NK, Schembri MA (2013) Chaperone-usher fimbriae of *Escherichia coli*. *PLoS One* 8:e52835.
22. Jones CH, et al. (1995) FimH adhesin of type 1 pili is assembled into a fibrillar tip structure in the Enterobacteriaceae. *Proc Natl Acad Sci USA* 92:2081–2085.
23. Mulvey MA, et al. (1998) Induction and evasion of host defenses by type 1-piliated uropathogenic *Escherichia coli*. *Science* 282:1494–1497.
24. Mydock-McGrane LK, Hannan TJ, Janetka JW (2017) Rational design strategies for FimH antagonists: New drugs on the horizon for urinary tract infection and Crohn's disease. *Expert Opin Drug Discov* 12:711–731.
25. Jarvis C, et al. (2016) Antivirulence isoquinolone mannosides: Optimization of the biaryl aglycone for FimH lectin binding affinity and efficacy in the treatment of chronic UTI. *ChemMedChem* 11:367–373.
26. Mydock-McGrane L, et al. (2016) Antivirulence C-mannosides as antibiotic-sparing, oral therapeutics for urinary tract infections. *J Med Chem* 59:9390–9408.
27. Han Z, et al. (2010) Structure-based drug design and optimization of mannoside bacterial FimH antagonists. *J Med Chem* 53:4779–4792.
28. Cusumano CK, et al. (2011) Treatment and prevention of urinary tract infection with orally active FimH inhibitors. *Sci Transl Med* 3:109ra115.
29. Grabosch C, Hartmann M, Schmidt-Lassen J, Lindhorst TK (2011) Squaric acid mono-amide mannosides as ligands for the bacterial lectin FimH: Covalent inhibition or not? *ChemBioChem* 12:1066–1074.
30. Kleeb S, et al. (2015) FimH antagonists: Bioisosteres to improve the in vitro and in vivo PK/PD profile. *J Med Chem* 58:2221–2239.
31. Chalopin T, et al. (2016) Second generation of thiazolylmannosides, FimH antagonists for *E. coli*-induced Crohn's disease. *Org Biomol Chem* 14:3913–3925.
32. Mydock-McGrane LK, Cusumano ZT, Janetka JW (2016) Mannose-derived FimH antagonists: A promising anti-virulence therapeutic strategy for urinary tract infections and Crohn's disease. *Expert Opin Ther Pat* 26:175–197.
33. Wurpel DJ, et al. (2014) F9 fimbriae of uropathogenic *Escherichia coli* are expressed at low temperature and recognise Galβ1-3GlcNAc-containing glycans. *PLoS One* 9: e93177.
34. Conover MS, et al. (2016) Inflammation-induced adhesin-receptor interaction provides a fitness advantage to uropathogenic *E. coli* during chronic infection. *Cell Host Microbe* 20:482–492.
35. Kalas V, et al. (2017) Evolutionary fine-tuning of conformational ensembles in FimH during host-pathogen interactions. *Sci Adv* 3:e1601944.
36. Le Trong I, et al. (2010) Structural basis for mechanical force regulation of the adhesin FimH via finger trap-like beta sheet twisting. *Cell* 141:645–655.
37. Sauer MM, et al. (2016) Catch-bond mechanism of the bacterial adhesin FimH. *Nat Commun* 7:10738.
38. Mayer K, et al. (2017) Urinary tract infection: Which conformation of the bacterial lectin FimH is therapeutically relevant? *J Med Chem* 60:5646–5662.
39. Hannan TJ, Mysorekar IU, Hung CS, Isaacson-Schmid ML, Hultgren SJ (2010) Early severe inflammatory responses to uropathogenic *E. coli* predispose to chronic and recurrent urinary tract infection. *PLoS Pathog* 6:e1001042.
40. Murawski IJ, et al. (2010) The C3H/HeJ inbred mouse is a model of vesico-ureteric reflux with a susceptibility locus on chromosome 12. *Kidney Int* 78:269–278.
41. Subashchandrabose S, et al. (2014) Host-specific induction of *Escherichia coli* fitness genes during human urinary tract infection. *Proc Natl Acad Sci USA* 111:18327–18332.
42. Bouckaert J, et al. (2006) The affinity of the FimH fimbrial adhesin is receptor-driven and quasi-independent of *Escherichia coli* pathotypes. *Mol Microbiol* 61:1556–1568.
43. Hung CS, et al. (2002) Structural basis of tropism of *Escherichia coli* to the bladder during urinary tract infection. *Mol Microbiol* 44:903–915.
44. Ernst B, Magnani JL (2009) From carbohydrate leads to glycomimetic drugs. *Nat Rev Drug Discov* 8:661–677.
45. Hsu CH, et al. (2016) The dependence of carbohydrate-aromatic interaction strengths on the structure of the carbohydrate. *J Am Chem Soc* 138:7636–7648.
46. Hudson KL, et al. (2015) Carbohydrate-aromatic interactions in proteins. *J Am Chem Soc* 137:15152–15160.
47. Ter Kuile BH, Kraupner N, Brul S (2016) The risk of low concentrations of antibiotics in agriculture for resistance in human health care. *FEMS Microbiol Lett* 363:fnw210.
48. Llor C, Bjerrum L (2014) Antimicrobial resistance: Risk associated with antibiotic overuse and initiatives to reduce the problem. *Ther Adv Drug Saf* 5:229–241.
49. Kardas P, Devine S, Golembesky A, Roberts C (2005) A systematic review and meta-analysis of misuse of antibiotic therapies in the community. *Int J Antimicrob Agents* 26:106–113.
50. Chang Q, Wang W, Regev-Yochay G, Lipsitch M, Hanage WP (2015) Antibiotics in agriculture and the risk to human health: How worried should we be? *Evol Appl* 8: 240–247.
51. Pinkner JS, et al. (2006) Rationally designed small compounds inhibit pilus biogenesis in uropathogenic bacteria. *Proc Natl Acad Sci USA* 103:17897–17902.
52. Trott O, Olson AJ (2010) AutoDock Vina: Improving the speed and accuracy of docking with a new scoring function, efficient optimization, and multithreading. *J Comput Chem* 31:455–461.
53. Irwin JJ, Sterling T, Mysinger MM, Bolstad ES, Coleman RG (2012) ZINC: A free tool to discover chemistry for biology. *J Chem Inf Model* 52:1757–1768.
54. O'Boyle NM, et al. (2011) Open Babel: An open chemical toolbox. *J Cheminform* 3:33.
55. Battye TG, Kontogiannis L, Johnson O, Powell HR, Leslie AG (2011) iMOSFLM: A new graphical interface for diffraction-image processing with MOSFLM. *Acta Crystallogr D Biol Crystallogr* 67:271–281.
56. Kabsch W (2010) Xds. *Acta Crystallogr D Biol Crystallogr* 66:125–132.
57. Winn MD, et al. (2011) Overview of the CCP4 suite and current developments. *Acta Crystallogr D Biol Crystallogr* 67:235–242.
58. Adams PD, et al. (2010) PHENIX: A comprehensive Python-based system for macromolecular structure solution. *Acta Crystallogr D Biol Crystallogr* 66:213–221.